

# Experimental electronic phase diagram in a diamond-lattice antiferromagnetic system

Liang-Wen Ji,<sup>1,\*</sup> Wu-Zhang Yang,<sup>2</sup> Yi-Ming Lu,<sup>1</sup> Jia-Yi Lu,<sup>1</sup> Jing Li,<sup>1</sup> Yi Liu,<sup>1,3</sup> Zhi Ren,<sup>2</sup> and Guang-Han Cao<sup>1,4,5,†</sup>

<sup>1</sup>*School of Physics, Zhejiang University, Hangzhou 310058, China*

<sup>2</sup>*School of Sciences, Westlake Institute for Advanced Study, Westlake University, Hangzhou 310064, China*

<sup>3</sup>*Department of Applied Physics, Zhejiang University of Technology, Hangzhou 310023, China*

<sup>4</sup>*Interdisciplinary Center for Quantum Information,*

*and State Key Laboratory of Silicon and Advanced Semiconductor Materials, Zhejiang University, Hangzhou 310058, China*

<sup>5</sup>*Collaborative Innovation Centre of Advanced Microstructures, Nanjing University, Nanjing, 210093, China*

(Dated: December 4, 2024)

We report Ni-doping effect on the magnetic and electronic properties of thiospinel  $\text{Co}_{1-x}\text{Ni}_x[\text{Co}_{0.3}\text{Ir}_{1.7}]\text{S}_4$  ( $0 \leq x \leq 1$ ). The parent compound  $\text{Co}[\text{Co}_{0.3}\text{Ir}_{1.7}]\text{S}_4$  exhibits antiferromagnetic order below  $T_N \sim 292$  K within the *A*-site diamond sublattice, along with a narrow charge-transfer gap. Upon Ni doping, an insulator-to-metal crossover occurs at  $x \sim 0.35$ , and the antiferromagnetism is gradually suppressed, with  $T_N$  decreasing to 23 K at  $x = 0.7$ . In the metallic state, a spin-glass-like transition emerges at low temperatures. The antiferromagnetic transition is completely suppressed at  $x_c \sim 0.95$ , around which a non-Fermi-liquid behavior emerges, evident from the  $T^\alpha$  temperature dependence with  $\alpha \approx 1.2$ - $1.3$  in resistivity and divergent behavior of  $C/T$  in specific heat at low temperatures. Meanwhile, the electronic specific heat coefficient  $\gamma$  increases substantially, signifying an enhancement of the quasiparticle effective mass. The magnetic phase diagram has been established, in which an antiferromagnetic quantum critical point is avoided at  $x_c$ . Conversely, the observed glass-like tail above the critical concentration aligns more closely with theoretical predictions for an extended region of quantum Griffiths phase in the presence of strong disorder.

PACS numbers: 72.80.Ga; 74.62.Dh; 75.30.-m; 74.70.Xa

## I. INTRODUCTION

Thiospinel compounds  $AB_2\text{S}_4$  have been extensively studied over the past few decades [1], displaying intricate phenomena such as superconductivity [2, 3], non-Fermi-liquid (NFL) behavior [4], metal-to-insulator transition [5], and orbital-glass state [6]. In particular, the complexity of magnetic thiospinels is intensified by frustration effects stemming from lattice geometry and competing exchange interactions [7–9]. The *A*-site diamond sublattice with only nearest-neighbor interactions is not geometrically frustrated for nearest-neighbor antiferromagnetic (AFM) ordering, in contrast with the case of *B*-site pyrochlore sublattice [8]. Nevertheless, competing higher-order neighboring interactions give rise to exotic ground states, including spin-orbital liquid near quantum criticality in  $\text{FeSc}_2\text{S}_4$  [10], spiral-spin liquid and antiferromagnetic skyrmions in  $\text{MnSc}_2\text{S}_4$  [11, 12], rendering *A*-site magnetic spinels of tremendous interest.

Recently, a new *A*-site magnetic spinel  $\text{Co}[\text{Co}_{0.3}\text{Ir}_{1.7}]\text{S}_4$  was discovered, featuring a high Néel temperature ( $T_N$ ) of 292 K [13]. Measurements of electrical resistivity and absorption spectrum show a narrow energy gap, which emerges between *Ir*- $t_{2g}$  orbitals and the antibonding states of *Co*- $t_2$  and *S*- $p$  orbitals. The narrow charge-transfer gap enables electron hopping between the unoccupied antibonding states of *Co*- $t_2$  and *S*- $p$  orbitals

via *Ir*- $t_{2g}$  states, thereby facilitating robust nearest-neighbor-coupled antiferromagnetism between the *Co*(*A*) ions with little magnetic frustrations.

AFM insulators can typically be manipulated by carrier doping, which adjusts the band filling and exerts a profound influence on both transport and magnetic properties [14, 15]. For example, Ni doping in iron-pnictide systems introduces excess itinerant electrons and suppresses the AFM order, leading to unconventional superconductivity (SC) [16, 17]. Likewise, Ni doping in  $\text{Co}[\text{Co}_{0.3}\text{Ir}_{1.7}]\text{S}_4$  can effectively introduce electron carriers. More importantly, electron doping will drive the antibonding states of *Co*- $t_2$  and *S*- $p$  orbitals to dominate the Fermi level, which seems to fulfill the electronic ‘gene’ for high-temperature SC [18, 19]. Thus, electron doping via Ni substitution may suppress the antiferromagnetism and trigger exotic phenomena in the cobalt thiospinel system.

In this study, we systematically investigated the effect of Ni substitution for *Co*(*A*) in  $\text{Co}_{1-x}\text{Ni}_x[\text{Co}_{0.3}\text{Ir}_{1.7}]\text{S}_4$  (abbreviated as  $\text{Co}_{1.3-x}\text{Ni}_x\text{Ir}_{1.7}\text{S}_4$ ) through x-ray diffraction (XRD), electrical transport, magnetic susceptibility and heat capacity measurements. Note that this is the first systematic study of electron doping in the diamond-lattice antiferromagnet  $\text{Co}_{1.3}\text{Ir}_{1.7}\text{S}_4$ . With increasing Ni concentration, an insulator-to-metal crossover (IMC) is induced and the AFM transition is gradually suppressed. Accompanied by the disappearance of AFM order, the resistivity and specific-heat data exhibit NFL behaviors at low temperatures, yet without SC. The phase diagram for  $\text{Co}_{1.3-x}\text{Ni}_x\text{Ir}_{1.7}\text{S}_4$  ( $0 \leq x \leq 1$ ) has been mapped out, suggesting a possible quantum Griffiths phase (QGP) at

\* lwji@zju.edu.cn

† ghcao@zju.edu.cn

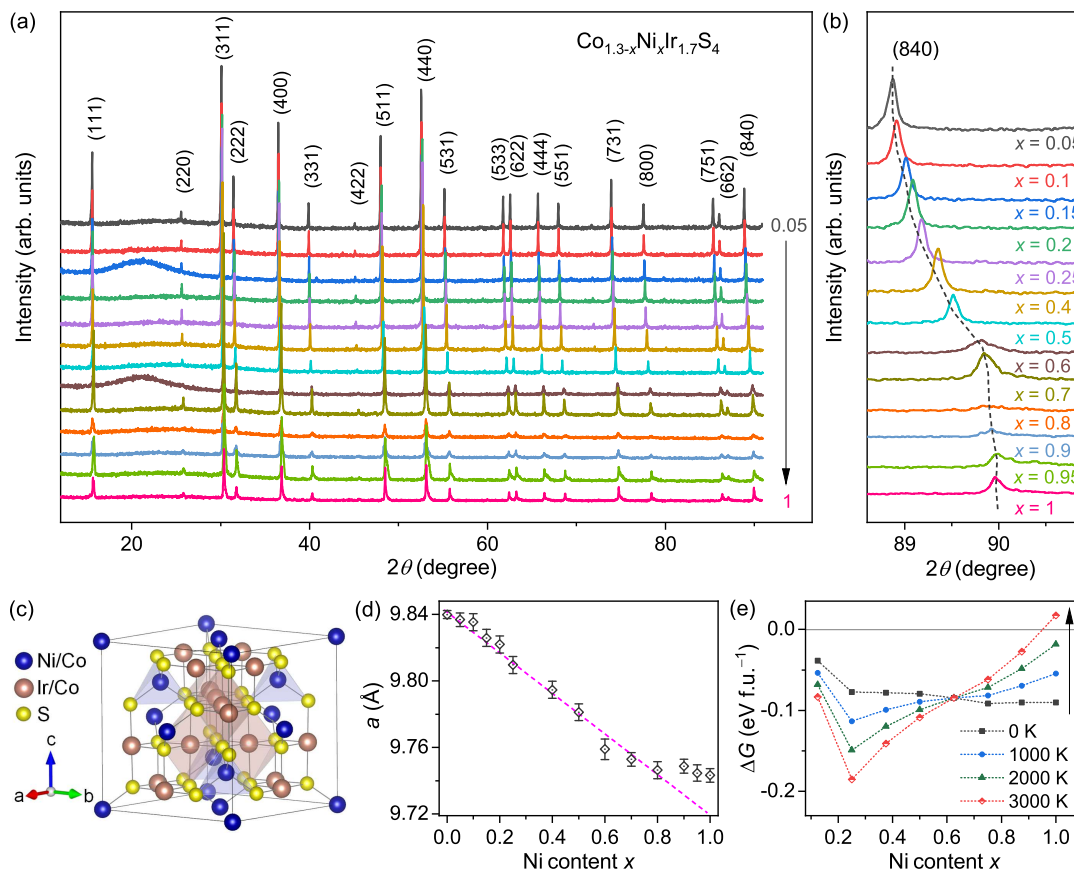


FIG. 1. (Color online) (a) Powder x-ray diffraction of  $\text{Co}_{1.3-x}\text{Ni}_x\text{Ir}_{1.7}\text{S}_4$ . (b) Diffraction peak of the (840) crystal plane. (c) Crystal structure of  $\text{Co}_{1.3-x}\text{Ni}_x\text{Ir}_{1.7}\text{S}_4$ . (d) Lattice parameter  $a$  as a function of Ni content. The dashed line is a guide to the eye. (e) Gibbs free energy difference between  $\text{Co}_{8-x}\text{Ni}_x[\text{Co}_2\text{Ir}_{14}\text{S}_{32}]$  (Co occupies B sites in prior, denoted as  $G_1$ ) and  $\text{Co}_{8-x+y}\text{Ni}_{x-y}[\text{Ni}_y\text{Co}_{2-y}\text{Ir}_{14}\text{S}_{32}]$  (Ni occupies B sites in prior, denoted as  $G_2$ ),  $\Delta G(T) = G_1(T) - G_2(T)$  with  $1 \leq x \leq 8$  and  $1 \leq y \leq 2$ .

$x > 0.95$ .

## II. METHODS

Polycrystalline samples of  $\text{Co}_{1.3-x}\text{Ni}_x\text{Ir}_{1.7}\text{S}_4$  ( $0 \leq x \leq 1$ ) were synthesized via a solid-state reaction using source materials of high-purity Ni powders (99.9%), Co powders (99.9%), Ir powders (99.95%), and S powders (99.99%). The nominal stoichiometric mixture of source materials was placed into a sealed evacuated quartz ampoule and slowly heated to 1223-1473 K for two days, depending on the Ni-doping level. The more Ni is introduced, the higher reaction temperature is needed. The resultant powder were reground and pressed, and then were heated to the same temperature for another two days. Note that all the operations of sample handling were carried out in a glove box filled with high-purity argon.

Powder XRD was carried out using a PANalytical x-ray diffractometer with monochromatic  $\text{Cu-K}\alpha_1$  radiation at room temperature. The lattice parameters were obtained by a least-squares fit of reflections in the range

of  $10^\circ \leq 2\theta \leq 90^\circ$ . The dc magnetization was carried out on a Quantum Design Magnetic Property Measurement System (MPMS3). The temperature dependence of electrical resistivity and heat capacity was measured on a Quantum Design Physical Property Measurement System (PPMS-9). A standard four-electrode method was employed for the resistivity measurement. The heat capacity was measured by a thermal relaxation method.

The density functional theory (DFT) calculations were performed using the Vienna Ab initio Simulation Package (VASP) [20] with the projector augmented-wave method [21]. The exchange-correlation energy was calculated with a Perdew-Burke-Ernzerhof (PBE) type functional [22]. The wave functions were expanded in the plane waves basis with an energy cutoff of 560 eV. A  $8 \times 8 \times 8$  and  $6 \times 6 \times 6$   $\Gamma$ -centered  $\mathbf{k}$  mesh was employed for calculations with the 14-atom primitive cell and 56-atom conventional cell, respectively. Conventional cells with varying Ni and Co occupancies were constructed to calculate their total enthalpy. Virtual crystal approximation (VCA) method was adopted to elucidate the change in the electronic structure induced by Ni doping [23].

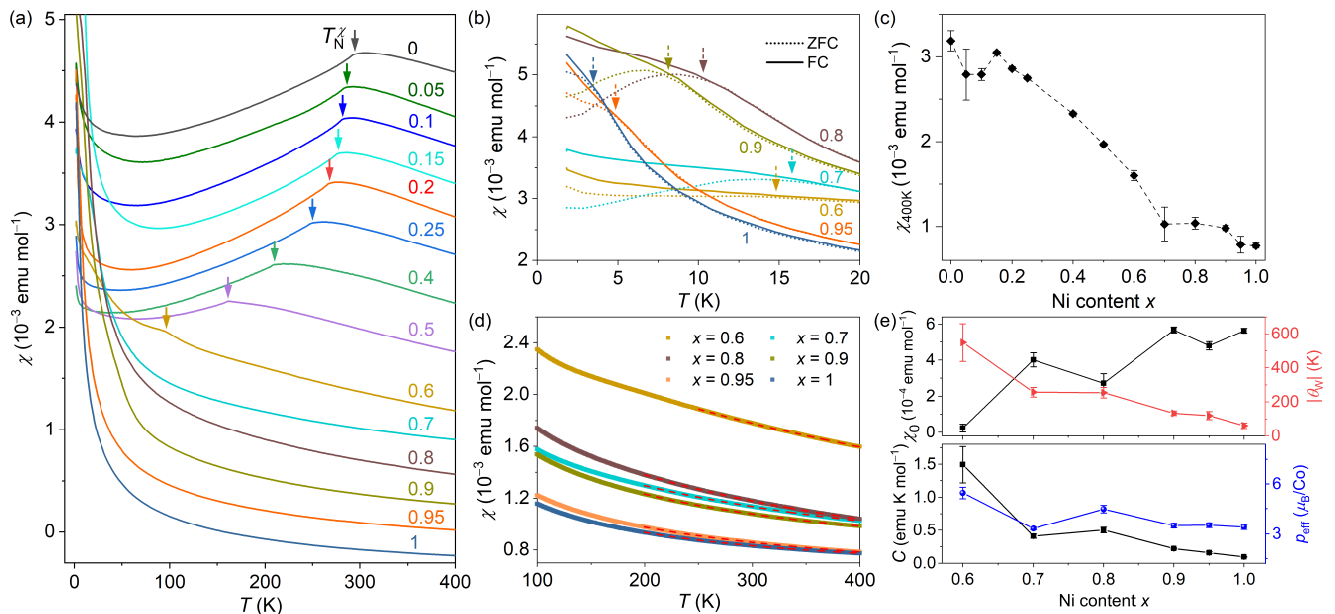


FIG. 2. (Color online) (a) Temperature dependence of magnetic susceptibility for  $\text{Co}_{1.3-x}\text{Ni}_x\text{Ir}_{1.7}\text{S}_4$  with  $0 \leq x \leq 1$ . The arrows represent the antiferromagnetic transition. The data are offset individually for clarity. (b) Temperature dependence of magnetic susceptibility in zero-field-cooling (ZFC) and field-cooling (FC) modes for  $\text{Co}_{1.3-x}\text{Ni}_x\text{Ir}_{1.7}\text{S}_4$  ( $0.6 \leq x \leq 1$ ), in which dashed arrows denote the spin-glass-like transition. (c) Magnetic susceptibility at 400 K ( $\chi_{400\text{K}}$ ) as a function of Ni content. (d) Magnetic susceptibility of  $\text{Co}_{1.3-x}\text{Ni}_x\text{Ir}_{1.7}\text{S}_4$  ( $0.6 \leq x \leq 1$ ) fitted with the Curie-Weiss formula. (e) The upper panel plots the temperature-independent term  $\chi_0$  (left axis) and the Weiss temperature  $\theta_W$  (right axis) as functions of Ni content  $x$ . The lower panel plots the Curie constant  $C$  (left axis) and corresponding effective magnetic moments per cobalt (right axis) as functions of Ni content  $x$ .

The nonmagnetic configurations were adopted in our calculations. All the crystal lattice and ionic sites of the primitive cell and conventional cell were fully relaxed.

### III. RESULTS AND DISCUSSION

#### A. Crystal structure

The XRD patterns of the series samples of  $\text{Co}_{1.3-x}\text{Ni}_x\text{Ir}_{1.7}\text{S}_4$  are shown in Fig. 1(a). Upon close inspection of the XRD pattern, it is evident that Ni doping leads to obvious shifts in the diffraction peaks (Fig. 1(b)). Nevertheless, the XRD reflections can be well indexed with the spinel structure in all Ni-concentrations. No secondary phase can be detected.

The dependence of unit-cell parameter on Ni content is shown in Fig. 1(d). The lattice constant  $a$  decreases from 9.840 Å for  $x = 0$  to 9.746 Å for  $x = 0.8$  at room temperature, showing a shrinkage of the lattice. In both normal  $\text{NiCo}_2\text{S}_4$  and inverse  $\text{Ni}_2\text{CoS}_4$  thiospinels, Co atoms preferentially occupy the  $B$  site [24, 25], which is consistent with crystal field stabilization energies [26]. To further clarify the preferences of Ni and Co for tetrahedral or octahedral sites in this system, we calculated the free energies of several specific configurations with different Ni and Co distributions (Table S1 in the SM [27]). As shown in Fig. 1(e), in most cases except

for  $x > 1$ , Ni residing at the  $A$  site and Co at the  $B$  site is indeed more stable. Therefore, substituting smaller  $\text{Ni}^{2+}$  (0.55 Å) for  $\text{Co}^{2+}$  (0.58 Å) at  $A$  site is expected to result in a decrease in unit-cell volume [28]. Here, the systematic change in  $a$  confirms Ni incorporation into the  $A$  site of the lattice.

In the range of  $0.8 < x \leq 1$ , however, the change of  $a$  deviates from a linear behavior. It is noted that the effective ionic radii for octahedrally coordinated  $\text{Ni}^{3+}$  (0.56 Å) is bigger than that of  $\text{Co}^{3+}$  (0.545 Å) [28]. Meanwhile, in the high-doping region, the free energy difference  $\Delta G$  between  $\text{Co}_{8-x}\text{Ni}_x[\text{Co}_2\text{Ir}_{14}]\text{S}_{32}$  and  $\text{Co}_{8-x+y}\text{Ni}_{x-y}[\text{Ni}_y\text{Co}_{2-y}\text{Ir}_{14}]\text{S}_{32}$  is minimized due to the increasing entropy contribution, implying a propensity toward site inversion. These phenomena suggest the disordered occupancy of Co and Ni at high doping levels. Furthermore, the deviation of  $a$  from the linear fit in Fig. 1(d) can be utilized to estimate the site inversion degree, which is approximately 4.6 % to 6.7 % for  $x \geq 0.9$  (Table S2 in the SM [27]).

#### B. Magnetic properties

Figure 2(a) shows the magnetic susceptibility  $\chi(T)$  of  $\text{Co}_{1.3-x}\text{Ni}_x\text{Ir}_{1.7}\text{S}_4$  samples. On cooling below room temperature, the parent compound  $\text{Co}_{1.3}\text{Ir}_{1.7}\text{S}_4$  exhibits a peak at  $T_N^x \sim 292$  K. With Ni doping, the  $\chi(T)$

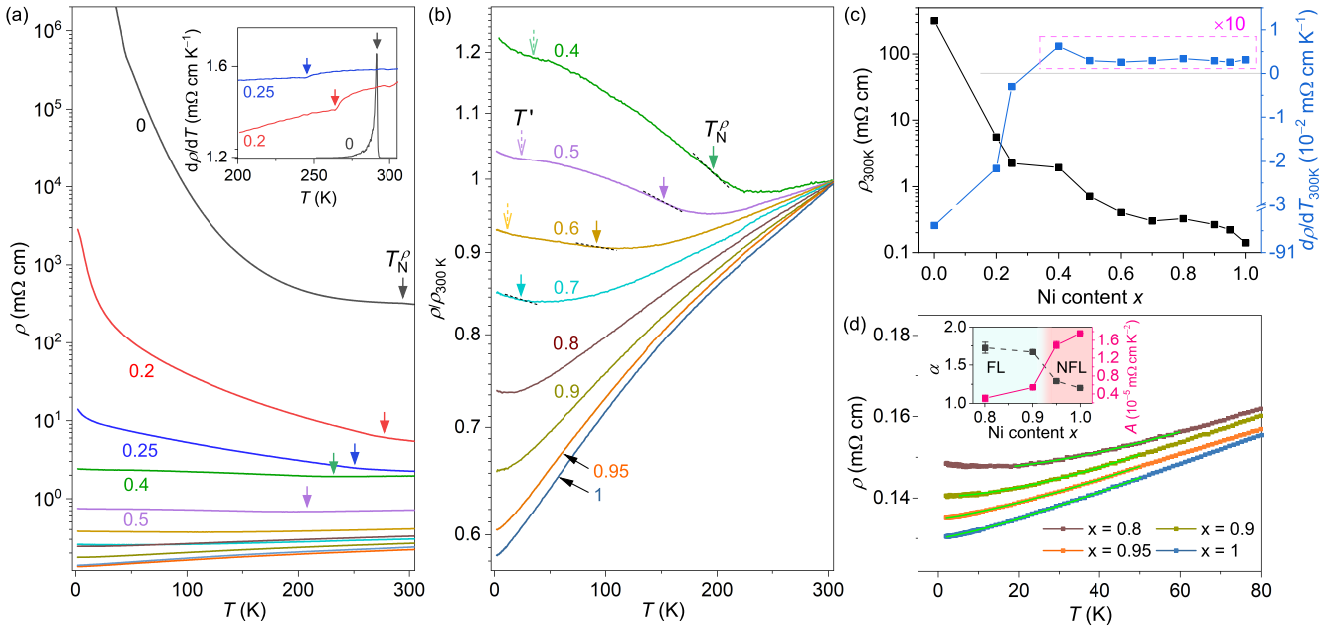


FIG. 3. (Color online) (a) Temperature dependence of electrical resistivity for the  $\text{Co}_{1.3-x}\text{Ni}_x\text{Ir}_{1.7}\text{S}_4$  polycrystalline samples. The inset is the corresponding  $d\rho/dT$  in the temperature range 200 to 310 K with an offset. (b) Temperature dependence of normalized resistivity of  $\text{Co}_{1.3-x}\text{Ni}_x\text{Ir}_{1.7}\text{S}_4$  ( $0.4 \leq x \leq 1$ ). The arrows and dashed arrows represent the antiferromagnetic ordering and low-temperature anomaly, respectively. (c) Resistivity at room temperature (left axis) and its derivative to temperature at 300 K (right axis) as functions of Ni content. The data in the dashed box are magnified by a factor of 10. (d) The low-temperature resistivity is fitted with the power law  $\rho = \rho_0 + AT^\alpha$ , with an offset applied for clarity. The inset plots exponent  $\alpha$  (left axis) and coefficient  $A$  of the  $T$ -square term in  $\rho = \rho_0 + AT^2$  (right axis) as functions of Ni content. Here, FL and NFL denotes Fermi liquid and non-Fermi liquid, respectively.

data exhibits an overall decline, as evidenced by the decrease of  $\chi_{400\text{K}}$  in Fig. 2(c). In the low-doping region ( $x \leq 0.6$ ), this AFM transition peak shifts to lower temperatures, indicating that the Néel temperature decreases gradually with increasing Ni content. As  $x$  increases to 0.6,  $T_N^X$  further reduces to  $\sim 95$  K, which is about 1/3 of the value for pristine  $\text{Co}_{1.3}\text{Ir}_{1.7}\text{S}_4$ . While at  $x \geq 0.7$ , no signature of AFM transition is observed, and the  $\chi(T)$  of  $\text{Co}_{1.3-x}\text{Ni}_x\text{Ir}_{1.7}\text{S}_4$  exhibits only Curie-Weiss paramagnetic behavior.

Upon careful examination of the low-temperature data,  $\chi(T)$  in zero-field-cooling and field-cooling modes bifurcate at  $x \geq 0.6$ , as illustrated in Fig. 2(b). This bifurcation behavior is reminiscent of a spin-glass-like transition, which is commonly observed in  $A$ -site magnetic spinels [29, 30]. Here, we define the bifurcation point as the spin-glass (SG) transition temperature  $T_{\text{SG}}$ , which also decreases with increasing  $x$ . Given a metallization at  $x \geq 0.6$  (see below), this SG-like behavior at low temperatures can be understood in terms of Ruderman–Kittel–Kasuya–Yosida (RKKY)-induced frustration [30].

At  $0.6 \leq x \leq 1$ , the paramagnetic behavior of  $\text{Co}_{1.3-x}\text{Ni}_x\text{Ir}_{1.7}\text{S}_4$  above 200 K (or 250 K) can be analyzed by the modified Curie-Weiss law,  $\chi = \chi_0 + C/(T - \theta_W)$  (Fig. 2(d)). The fitted parameters as functions of Ni content are shown in Fig. 2(e). The

temperature-independent term  $\chi_0$  increases with increasing Ni concentration, consistent with the nearly unchanged core-electron diamagnetism and increasing Pauli paramagnetism ( $\chi_P = \mu_B^2 N(E_F)$ , see below). The absolute value of the Weiss temperature  $|\theta_W|$  decreases gradually, indicating the diluted magnetic interaction with Ni doping. The Curie constant  $C$  also shows a decreasing trend, which can be basically explained by the nonmagnetic (NM) nature of Ni ions at the  $A$  site. Numerically, the decrease of  $\chi_{400\text{K}}$  should be primarily contributed by the reduced Curie-Weiss paramagnetism.

Unlike the NM  $\text{NiIr}_2\text{S}_4$  [31],  $\text{Co}_{0.3}\text{NiIr}_{1.7}\text{S}_4$  exhibits a notably large magnetic moment of  $p_{\text{eff}} \sim 0.8 \mu_B$  f.u.<sup>-1</sup>. Considering that only  $\text{Co}^{2+}$  ions generate magnetic moments, we present the Curie-Weiss paramagnetism signal per Co ion on the basis of the site inversion, as depicted in the lower panel of Fig. 2(e). At  $x = 0.6$ , the local moment per Co ion is  $\sim 5.48 \mu_B$ , comparable to that of pristine  $\text{Co}_{1.3}\text{Ir}_{1.7}\text{S}_4$  [13]. In the range of  $0.6 \leq x \leq 0.9$ , a general decline in the local moment per Co ion is observed. For  $x \geq 0.9$ , the local moment is approximately  $3.4 \mu_B/\text{Co}$ , showing little dependence on Ni content.



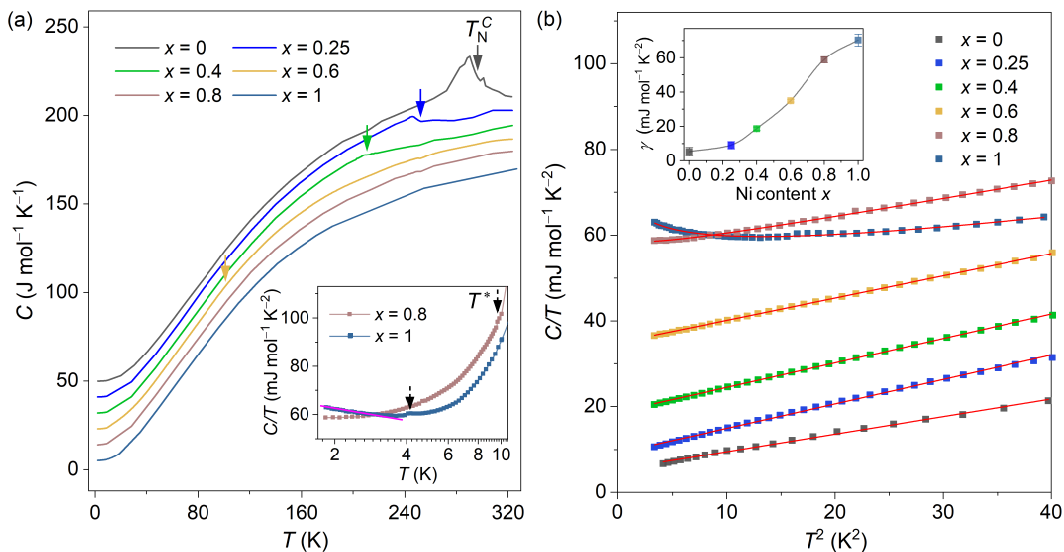


FIG. 4. (Color online) (a) Temperature dependence of specific heat  $C$  for  $\text{Co}_{1.3-x}\text{Ni}_x\text{Ir}_{1.7}\text{S}_4$ . The data are shifted upward one by one for clarity. The inset shows logarithmic temperature dependence of  $C/T$  at low temperatures, with the dashed arrows indicating the anomalies. (b)  $C/T$  versus  $T^2$  at low temperatures. The inset plots the electronic specific heat coefficient as a function of Ni content.

### C. Electrical resistivity

Figures 3(a) and 3(b) show the temperature dependence of electrical resistivity for  $\text{Co}_{1.3-x}\text{Ni}_x\text{Ir}_{1.7}\text{S}_4$ . The resistivity of  $\text{Co}_{1.3}\text{Ir}_{1.7}\text{S}_4$  exhibits an insulating behavior, with a sharp peak in  $d\rho/dT$ , coincident with the AFM transition at 292 K (inset of Fig. 3(a)). Upon Ni doping, the insulating property is gradually suppressed, as evidenced by  $\rho(T)$  plummeting by several orders of magnitude at  $x = 1$ . As shown in Fig. 3(c),  $\rho_{300\text{K}}$  decreases by more than 3 orders of magnitude, falling below 1 m $\Omega$  cm at  $x \geq 0.5$ . Concurrently,  $d\rho/dT$  at room temperature changes sign at  $x \approx 0.35$ , suggesting an IMC (Fig. 3(c)). In the insulating state, the resistivity of  $\text{Co}_{1.3-x}\text{Ni}_x\text{Ir}_{1.7}\text{S}_4$  exhibits a concave anomaly around the AFM transition, allowing one to trace the evolution of magnetic order.

At  $x \geq 0.4$ , the resistivity of  $\text{Co}_{1.3-x}\text{Ni}_x\text{Ir}_{1.7}\text{S}_4$  exhibits metallic behavior, accompanied by an obvious upturn at low temperatures (Fig. 3(b)). The low-temperature upturn behavior is also observed in other 3d transition-metal compounds, typically attributed to the localization or Kondo effect [32, 33]. Notably, the upturn transition of  $\text{Co}_{1.3-x}\text{Ni}_x\text{Ir}_{1.7}\text{S}_4$  evolves from the Mott-like transition within this system, thus it can be reasonably attributed to the establishment of AFM order. Here, we denote the temperature corresponding to the inflection point of resistivity as  $T_N^{\rho}$ , which also decreases as Ni content increases. The AFM ordering persists for Ni concentrations of  $0.6 \leq x \leq 0.9$ . Note that, at  $0.4 \leq x \leq 0.6$ , another upturn emerges at low temperatures, denoted as  $T'$  and marked by dashed arrows in Fig. 3(b), which coincides with the SG-like

transition. The closeness between  $T'$  and  $T_{\text{SG}}$  suggests that these transitions may originate from similar cobalt spins. That is to say, there should be a re-entrant SG transition below the AFM ordering temperature.

At  $x > 0.9$ ,  $\text{Co}_{1.3-x}\text{Ni}_x\text{Ir}_{1.7}\text{S}_4$  is metallic across the entire temperature range, with no magnetic anomalies observed. On the other hand, the low-temperature resistivity exhibits a power-law behavior (Fig. 3(d)). The power exponent  $\alpha$  intriguingly reveals two regimes, as indicated in the inset of Fig. 3(d). At  $x \leq 0.9$ , the resistivity exhibits a clear power-law behavior with  $\alpha \sim 1.7$  at low temperatures, which is close to the Fermi-liquid (FL) scenario characterized by  $\alpha = 2$ . While at  $x \geq 0.95$ ,  $\alpha$  ranges from 1.2 to 1.3. The significant deviation from  $T^2$  dependence suggests NFL behavior in  $\text{Co}_{1.3-x}\text{Ni}_x\text{Ir}_{1.7}\text{S}_4$ , which is rare in spinel [1, 4]. Here we note that, if assuming a Fermi liquid in the low-temperature limit, the fitted coefficient  $A$  of the  $T^2$  term is found to increase substantially, indicating the increase of effective mass of conduction electrons.

In chemical substitution systems, disorder plays a crucial role in triggering NFL behavior [34]. Particularly in disorder-driven heavy fermion systems, SG freezing is often accompanied by the emergence of NFL behavior [34, 35]. In this context, the SG-like behavior observed in magnetic and resistivity measurements suggests a significant impact of disorder. Meanwhile, NFL behavior has not been observed in  $\text{NiIr}_2\text{S}_4$  (Figure S1 in the SM [27]). Thus, the presence of site inversion between Co and Ni atoms may contribute to the exotic NFL in Co-doped  $\text{NiIr}_2\text{S}_4$ .

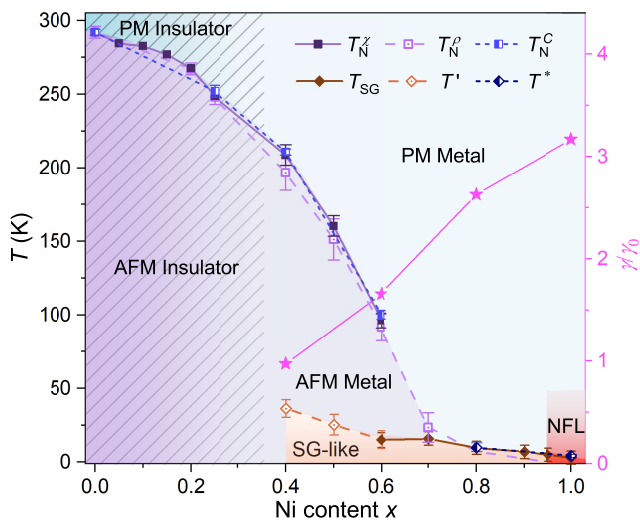


FIG. 5. (Color online) Phase diagram of  $\text{Co}_{1.3-x}\text{Ni}_x\text{Ir}_{1.7}\text{S}_4$  ( $0 \leq x \leq 1$ ).  $T_N^x$  and  $T_{\text{SG}}$  are deduced from magnetic data,  $T_N^{\rho}$  and  $T'$  are obtained from resistivity data, while  $T_N^C$  and  $T^*$  are from heat capacity data. PM Insulator, AFM Insulator, PM Metal, AFM Metal, SG-like, and NFL denote paramagnetic insulator, antiferromagnetic insulator, paramagnetic metal, antiferromagnetic metal, spin-glass-like, and non-Fermi-liquid, respectively. The right axis plots the ratio of the electronic specific-heat coefficient from experimental results ( $\gamma$ ) to DFT calculations ( $\gamma_0$ ).

#### D. Heat capacity

Figure 4(a) shows the specific heat  $C(T)$  for the  $\text{Co}_{1.3-x}\text{Ni}_x\text{Ir}_{1.7}\text{S}_4$  samples with  $x = 0, 0.25, 0.4, 0.6, 0.8$  and 1. The AFM ordering is confirmed by the peak at  $T_N^C$ , as remarked by the arrows in Fig. 4(a). The Néel temperature decreases with increasing  $x$ , consistent with the magnetic and resistive measurements above. Meanwhile, the magnetic related peak progressively weakens with increasing Ni content, suggesting a corresponding reduction in entropy change. This implies a decrease in the local moment, consistent with the fitted Curie constants. As  $x$  increases up to 0.8,  $C(T)$  shows no signature of AFM transition at high temperatures, but exhibits a low-temperature anomaly (inset of Fig. 4(a)), coinciding with the magnetic susceptibility bifurcation shown in Fig. 2(b). For  $x = 1$ , the  $C/T$  data displays a distinct logarithmic  $T$  dependence, as guided by the solid line in the inset of Fig. 4(a), aligning with the NFL behavior. The anomaly corresponding to the SG-like transition persists.

Figure 4(b) shows the plots of  $C/T$  versus  $T^2$  at low temperatures. At  $0 \leq x \leq 0.6$ , a linear relation between  $C/T$  and  $T^2$  exists, reflecting the dominant contributions from the phonon and AFM magnon part ( $\beta T^3$ ) and the electronic part  $\gamma T$ . While at higher Ni concentration ( $x > 0.8$ ), the  $-T \ln T$  contribution from electron-electron interactions should also be taken into consideration [36]. Therefore,  $C/T = \gamma + \beta T^2$  and

$C/T = \gamma + \beta T^2 - \eta \ln T$  are used for fitting the low-temperature data of  $\text{Co}_{1.3-x}\text{Ni}_x\text{Ir}_{1.7}\text{S}_4$  with  $0 \leq x \leq 0.6$  and  $0.8 \leq x \leq 1$ , respectively.

The dependence of  $\gamma$  on Ni content is shown in the inset of Fig. 4(b). The electronic specific heat coefficient  $\gamma$  increases continuously up to  $x = 1$ . More importantly, for  $x \geq 0.6$ ,  $\gamma$  of  $\text{Co}_{1.3-x}\text{Ni}_x\text{Ir}_{1.7}\text{S}_4$  surpasses that of the NM metallic  $\text{NiIr}_2\text{S}_4$  (Figure S2 in the SM [27]). In contrast to  $\text{NiIr}_2\text{S}_4$  governed by Fermi-liquid theory, the significantly elevated  $\gamma$  of  $\text{Co}_{1.3-x}\text{Ni}_x\text{Ir}_{1.7}\text{S}_4$  around  $x = 1$  indicates an enhanced effective mass  $m^*$ , as also indicated by the coefficient  $A$ , which is possibly associated with spin fluctuations near the suppression of magnetic order [37, 38].

#### E. Phase diagram

With the results above, we mapped out the phase diagram of  $\text{Co}_{1.3-x}\text{Ni}_x\text{Ir}_{1.7}\text{S}_4$  (Fig. 5), unveiling a fascinating evolution of the electronic and magnetic properties upon Ni doping.  $\text{Co}_{1.3-x}\text{Ni}_x\text{Ir}_{1.7}\text{S}_4$  alters from an insulator at  $x \leq 0.25$  to a metal at  $x \geq 0.4$ , with the IMC occurring at  $x \approx 0.35$ . As the Ni concentration increases, the AFM transition is gradually suppressed in both the insulating and metallic states, with the Néel temperature decreasing from 292 K at  $x = 0$  to 23 K at  $x = 0.7$ . The AFM transition temperatures determined from magnetic susceptibility ( $T_N^x$ ), resistivity ( $T_N^{\rho}$ ) and specific heat ( $T_N^C$ ) are generally consistent. In the region of  $x \geq 0.4$ , a SG-like transition appears at  $T'$ ,  $T_{\text{SG}}$  or  $T^*$ . All three temperatures ( $T'$ ,  $T_{\text{SG}}$  and  $T^*$ ) decrease with increasing  $x$  and coincide with each other. At  $x \geq 0.95$ , the AFM ordering vanishes, leaving only the SG anomaly at low temperatures. Notably, NFL behavior emerges within this doping range.

To further elucidate the anomalous physical properties exhibited, we performed DFT calculations on the electronic structure of  $\text{Co}_{1.3-x}\text{Ni}_x\text{Ir}_{1.7}\text{S}_4$  with  $0.4 \leq x \leq 1$  (Figures S3 and S4 in the SM [27]).  $\text{Co}_{1.3-x}\text{Ni}_x\text{Ir}_{1.7}\text{S}_4$  remains in a metallic state, with the Fermi energy  $E_F$  locates at a valley in the total density of states (DOS). From  $x = 0.4$  to  $x = 1$ ,  $E_F$  shift to the right due to the doping of 0.6 extra electrons, resulting in a slight increase of the DOS at  $E_F$ . From the bare DOS at  $E_F$  ( $N(E_F)$ ), an electronic specific-heat coefficient of  $\gamma_0 = \frac{1}{3}\pi^2 k_B^2 N(E_F)$  can be estimated (Fig. 5). At  $x = 0.4$ , the derived  $\gamma_0$  precisely matches the experimental value. However, the significantly underestimated  $\gamma_0$  fails to explain the elevated experimental  $\gamma$  for  $x \geq 0.6$ . The band structure of  $\text{Co}_{1.3-x}\text{Ni}_x\text{Ir}_{1.7}\text{S}_4$  exhibits relatively flat dispersions along the X-W line, with narrow bands gradually approaching  $E_F$  as  $x$  increases (Figure S4 in the SM [27]). Thus, the discrepancy between  $\gamma_0$  and  $\gamma$  may suggest the effective mass renormalization primarily arises from electron-electron interactions [39, 40]. Particularly, the enhanced electron correlations are crucial for the breakdown of Fermi-liquid

in  $\text{Co}_{1.3-x}\text{Ni}_x\text{Ir}_{1.7}\text{S}_4$  [36].

In the vicinity of the AFM critical region around  $x_c = 0.95$ , the enhancement of quasiparticle scattering and effective mass implies the possibility of proximity to quantum criticality [36]. Nonetheless, rather than an AFM quantum critical point (QCP) at the critical concentration, the SG-like transition retains a ‘tail’ for  $x > x_c$ , which is typically observed in disordered systems [36, 41]. Notably, the magnetic moment and  $\theta_W$  of  $\text{Co}_{1.3-x}\text{Ni}_x\text{Ir}_{1.7}\text{S}_4$  remain nonzero up to  $x = 1$ , as revealed by magnetic susceptibility. Additionally, the NFL behavior persists in an extended region beyond  $x_c$  (see Figure S1 in the SM [27]). Resembling the  $\text{MnSi}$ ,  $\text{Ni}_{1-y}\text{V}_y$  or  $\text{Mn}_{1-x}\text{Fe}_x\text{Si}$  systems [42–44], an infinite-randomness QCP is likely induced by the strong disorder in this system, with a QGP potentially emerging above  $x_c$  [41]. The inherent disorder also probably inhibits SC near the quantum critical region [45].

Within a quantum Griffiths region, power-law singularities of many observables, including magnetic susceptibility, specific heat, and zero-temperature magnetization are predicted [46]. A power-law fit ( $T^{-\eta}$  or  $H^\eta$ ) to  $\chi(T)$ ,  $M(H)$  at 4 K and  $\Delta C/T$  for  $\text{Co}_{0.3}\text{NiIr}_{1.7}\text{S}_4$  yields  $\eta$  values of 0.51, 0.8 and 0.42, respectively (Figure S5 in the SM [27]), which are comparable to those exhibiting NFL behavior due to a QGP [35]. In addition,  $(M/H)T^\eta$  versus  $H/T^\delta$  with  $\eta = 0.46$  and  $\delta = 1.32$  can generally be collapsed onto a single curve [47, 48]. Therefore, the subtle interplay of randomness and quantum fluctuations at low temperatures is considered to give rise to the NFL in this system. Further investigations are still needed to ascertain whether quantum Griffiths singularity or

related effects are indeed present in this system.

#### IV. CONCLUDING REMARKS

We successfully synthesized single-phase samples of thiospinel  $\text{Co}_{1.3-x}\text{Ni}_x\text{Ir}_{1.7}\text{S}_4$  ( $0 \leq x \leq 1$ ). The gradual incorporation of Ni at the Co(A) site leads to an IMC around  $x = 0.35$ , the emergence of SG-like behavior at  $x \geq 0.4$  and the suppression of AFM order at the critical concentration of  $x_c \approx 0.95$ . Subsequent to the collapse of AFM order, NFL behavior and a substantial increase of the effective mass are observed. Nevertheless, the phase diagram of  $\text{Co}_{1.3-x}\text{Ni}_x\text{Ir}_{1.7}\text{S}_4$  reveals an extended SG-like tail beyond  $x_c$ , with properties possibly indicative of a QGP at low temperatures due to the randomness generated by strong disorder. The details of quantum Griffiths phase above  $x_c$  will need to be further resolved. Overall, our results provide insights into magnetic quantum criticality with the interplay of quenched disorder in this correlated Co-based diamond-lattice antiferromagnets.

#### ACKNOWLEDGMENTS

This work was supported by the National Key Research and Development Program of China (2022YFA1403202, 2023YFA1406101), and the National Natural Science Foundation of China (12050003), and the Key Research and Development Program of Zhejiang Province, China (2021C01002).

#### REFERENCES

- 
- [1] V. Tsurkan, H.-A. K. Von Nidda, J. Deisenhofer, P. Lunkenheimer, and A. Loidl, On the complexity of spinels: Magnetic, electronic, and polar ground states, *Phys. Rep.* **926**, 1 (2021).
  - [2] T. Hagino, Y. Seki, N. Wada, S. Tsuji, T. Shirane, K. I. Kumagai, and S. Nagata, Superconductivity in spinel-type compounds  $\text{CuRh}_2\text{S}_4$  and  $\text{CuRh}_2\text{Se}_4$ , *Phys. Rev. B* **51**, 12673 (1995).
  - [3] Y.-Y. Jin, S.-H. Sun, Y.-W. Cui, Q.-Q. Zhu, L.-W. Ji, Z. Ren, and G.-H. Cao, Bulk superconductivity and Pauli paramagnetism in nearly stoichiometric  $\text{CuCo}_2\text{S}_4$ , *Phys. Rev. Mater.* **5**, 074804 (2021).
  - [4] J. Huang, L. Chen, Y. Huang, C. Setty, B. Gao, Y. Shi, Z. Liu, Y. Zhang, T. Yilmaz, E. Vescovo, *et al.*, Non-Fermi liquid behaviour in a correlated flat-band pyrochlore lattice, *Nat. Phys.* , 1 (2024).
  - [5] P. G. Radaelli, Y. Horibe, M. J. Gutmann, H. Ishibashi, C. Chen, R. M. Ibberson, Y. Koyama, Y.-S. Hor, V. Kiryukhin, and S.-W. Cheong, Formation of isomorphic  $\text{Ir}^{3+}$  and  $\text{Ir}^{4+}$  octamers and spin dimerization in the spinel  $\text{CuIr}_2\text{S}_4$ , *Nature* **416**, 155 (2002).
  - [6] R. Fichtl, V. Tsurkan, P. Lunkenheimer, J. Hemberger, V. Fritsch, H.-A. KrugvonNidda, E.-W. Scheidt, and A. Loidl, Orbital Freezing and Orbital Glass State in  $\text{FeCr}_2\text{S}_4$ , *Phys. Rev. Lett.* **94**, 027601 (2005).
  - [7] M. Harris and M. Zinkin, Frustration in the pyrochlore antiferromagnets, *Mod. Phys. Lett. B* **10**, 417 (1996).
  - [8] L. Balents, Spin liquids in frustrated magnets, *Nature* **464**, 199 (2010).
  - [9] D. Bergman, J. Alicea, E. Gull, S. Trebst, and L. Balents, Order-by-disorder and spiral spin-liquid in frustrated diamond-lattice antiferromagnets, *Nat. Phys.* **3**, 487 (2007).
  - [10] K. W. Plumb, J. R. Morey, J. A. Rodriguez-Rivera, H. Wu, A. A. Podlesnyak, T. M. McQueen, and C. L. Broholm, Antiferromagnetic and orbital ordering on a diamond lattice near quantum criticality, *Phys. Rev. X* **6**, 041055 (2016).
  - [11] S. Gao, O. Zaharko, V. Tsurkan, Y. Su, J. S. White, G. S. Tucker, B. Roessli, F. Bourdarot, R. Sibille, D. Chernyshov, *et al.*, Spiral spin-liquid and the emergence of a vortex-like state in  $\text{MnSc}_2\text{S}_4$ , *Nat. Phys.* **13**, 157 (2017).

- [12] S. Gao, H. D. Rosales, F. A. Gomez Albarracin, V. Tsurkan, G. Kaur, T. Fennell, P. Steffens, M. Boehm, P. Čermák, A. Schneidewind, *et al.*, Fractional antiferromagnetic skyrmion lattice induced by anisotropic couplings, *Nature* **586**, 37 (2020).
- [13] L.-W. Ji, S.-Q. Wu, B.-Z. Li, W.-Z. Yang, S.-J. Song, Y. Liu, J. Li, Z. Ren, and G.-H. Cao, Inter-cation charge transfer mediated antiferromagnetism in  $\text{Co}_{1+x}\text{Ir}_{2-x}\text{S}_4$ , *Phys. Rev. B* **110**, 155139 (2024).
- [14] M. Imada, A. Fujimori, and Y. Tokura, Metal-insulator transitions, *Rev. Mod. Phys.* **70**, 1039 (1998).
- [15] D. I. Khomskii, *Transition metal compounds* (Cambridge University Press, 2014).
- [16] G. Cao, S. Jiang, X. Lin, C. Wang, Y. Li, Z. Ren, Q. Tao, C. Feng, J. Dai, Z. Xu, *et al.*, Narrow superconducting window in  $\text{LaFe}_{1-x}\text{Ni}_x\text{AsO}$ , *Phys. Rev. B* **79**, 174505 (2009).
- [17] L. Li, Y. Luo, Q. Wang, H. Chen, Z. Ren, Q. Tao, Y. Li, X. Lin, M. He, Z. Zhu, *et al.*, Superconductivity induced by Ni doping in  $\text{BaFe}_2\text{As}_2$  single crystals, *New J. Phys.* **11**, 025008 (2009).
- [18] J. Hu and C. Le, A possible new family of unconventional high temperature superconductors, *Sci. Bull.* **62**, 212 (2017).
- [19] J. Hu, Y. Gu, and C. Le, Predicting diamond-like Co-based chalcogenides as unconventional high temperature superconductors, *Sci. Bull.* **63**, 1338 (2018).
- [20] G. Kresse and J. Furthmüller, Efficient iterative schemes for ab initio total-energy calculations using a plane-wave basis set, *Phys. Rev. B* **54**, 11169 (1996).
- [21] P. E. Blöchl, Projector augmented-wave method, *Phys. Rev. B* **50**, 17953 (1994).
- [22] J. P. Perdew, K. Burke, and M. Ernzerhof, Generalized gradient approximation made simple, *Phys. Rev. Lett.* **77**, 3865 (1996).
- [23] L. Bellaïche and D. Vanderbilt, Virtual crystal approximation revisited: Application to dielectric and piezoelectric properties of perovskites, *Phys. Rev. B* **61**, 7877 (2000).
- [24] O. Knop, K. I. Reid, Sutarno, and Y. Nakagawa, Chalcogenides of the transition elements. VI. X-Ray, neutron, and magnetic investigation of the spinels  $\text{Co}_3\text{O}_4$ ,  $\text{NiCo}_2\text{O}_4$ ,  $\text{Co}_3\text{S}_4$ , and  $\text{NiCo}_2\text{S}_4$ , *Can. J. Chem.* **46**, 3463 (1968).
- [25] C.-H. Huang and O. Knop, Chalkogenides of the transition elements. VIII. An X-ray and neutron diffraction study of the spinel  $\text{CoNi}_2\text{S}_4$ , *Can. J. Chem.* **49**, 598 (1971).
- [26] U. Muller, *Inorganic structural chemistry* (John Wiley & Sons, 2007).
- [27] See Supplemental Material at [URL] for the free energy difference between  $\text{Co}_{8-x}\text{Ni}_x[\text{Co}_2\text{Ir}_{14}]\text{S}_{32}$  and  $\text{Co}_{8-x+y}\text{Ni}_{x-y}[\text{Ni}_y\text{Co}_{2-y}\text{Ir}_{14}]\text{S}_{32}$  ( $1 \leq x \leq 8$ ,  $1 \leq y \leq 2$ ), the estimation of site inversion degree, the resistivity of  $\text{NiIr}_2\text{S}_4$  and  $\text{Co}_{1.3-x}\text{Ni}_x\text{Ir}_2\text{S}_4$  ( $0.95 \leq x \leq 1.15$ ), the specific heat of  $\text{NiIr}_2\text{S}_4$ , the density of states and band structure for  $\text{Co}_{1-x}\text{Ni}_x[\text{Co}_{0.3}\text{Ir}_{1.7}]\text{S}_4$  ( $0.4 \leq x \leq 1$ ) and the magnetic susceptibility, isothermal magnetization and specific heat for  $\text{Co}_{0.3}\text{NiIr}_{1.7}\text{S}_4$ .
- [28] R. D. Shannon, Revised effective ionic radii and systematic studies of interatomic distances in halides and chalcogenides, *Acta Crystallogr. A* **32**, 751 (1976).
- [29] C. P. Poole Jr and H. A. Farach, Magnetic phase diagram of spinel spin-glasses, *Z. Phys. B: Condens. Matter* **47**, 55 (1982).
- [30] T. Naka, J. Valenta, T. Nakane, S. Ishii, M. Nakayama, H. Mamiya, K. Takehana, N. Tsujii, Y. Imanaka, Y. Matsushita, *et al.*, Phase transitions and slow spin dynamics of slightly inverted A-site spinel  $\text{CoAl}_{2-x}\text{Ga}_x\text{O}_4$ , *J. Phys. Condens. Matter* **36**, 125801 (2023).
- [31] R. Endoh, N. Matsumoto, S. Chikazawa, S. Nagata, T. Furubayashi, and T. Matsumoto, Metal-insulator transition in the spinel-type  $\text{Cu}_{1-x}\text{Ni}_x\text{Ir}_2\text{S}_4$  system, *Phys. Rev. B* **64**, 075106 (2001).
- [32] F. Rullier-Albenque, H. Alloul, and R. Tourbot, Disorder and transport in cuprates: weak localization and magnetic contributions, *Phys. Rev. Lett.* **87**, 157001 (2001).
- [33] G.-M. Zhang, Y.-F. Yang, and F.-C. Zhang, Self-doped Mott insulator for parent compounds of nickelate superconductors, *Phys. Rev. B* **101**, 020501(R) (2020).
- [34] E. Miranda and V. Dobrosavljević, Disorder-driven non-Fermi liquid behaviour of correlated electrons, *Rep. Prog. Phys.* **68**, 2337 (2005).
- [35] G. Stewart, Non-Fermi-liquid behavior in d-and f-electron metals, *Rev. Mod. Phys.* **73**, 797 (2001).
- [36] H. v. Löhneysen, A. Rosch, M. Vojta, and P. Wölfle, Fermi-liquid instabilities at magnetic quantum phase transitions, *Rev. Mod. Phys.* **79**, 1015 (2007).
- [37] B. Michon, C. Girod, S. Badoux, J. Kačmarčík, Q. Ma, M. Dragomir, H. Dabkowska, B. Gaulin, J.-S. Zhou, S. Pyon, *et al.*, Thermodynamic signatures of quantum criticality in cuprate superconductors, *Nature* **567**, 218 (2019).
- [38] O. Grossman, J. S. Hofmann, T. Holder, and E. Berg, Specific heat of a quantum critical metal, *Phys. Rev. Lett.* **127**, 017601 (2021).
- [39] J. Huang, L. Chen, Y. Huang, C. Setty, B. Gao, Y. Shi, Z. Liu, Y. Zhang, T. Yilmaz, E. Vescovo, *et al.*, Non-Fermi liquid behaviour in a correlated flat-band pyrochlore lattice, *Nature Physics*, 1 (2024).
- [40] Y. Liu, Z.-Y. Liu, J.-K. Bao, P.-T. Yang, L.-W. Ji, S.-Q. Wu, Q.-X. Shen, J. Luo, J. Yang, J.-Y. Liu, *et al.*, Superconductivity under pressure in a chromium-based kagome metal, *Nature* **632**, 1032 (2024).
- [41] T. Vojta, Quantum Griffiths effects and smeared phase transitions in metals: Theory and experiment, *J. Low Temp. Phys.* **161**, 299 (2010).
- [42] C. Pfleiderer, P. Boni, T. Keller, U. Rossler, and A. Rosch, Non-Fermi liquid metal without quantum criticality, *Science* **316**, 1871 (2007).
- [43] S. Ubaid-Kassis, T. Vojta, and A. Schroeder, Quantum Griffiths Phase in the Weak Itinerant Ferromagnetic Alloy  $\text{Ni}_{1-x}\text{V}_x$ , *Phys. Rev. Lett.* **104**, 066402 (2010).
- [44] A. K. Mishra, S. S. Samatham, M. T. F. Telling, A. D. Hillier, M. R. Lees, K. G. Suresh, and V. Ganesan, Quantum Griffiths phase in disordered  $\text{Mn}_{1-x}\text{Fe}_x\text{Si}$ , *Phys. Rev. B* **107**, L100405 (2023).
- [45] G. Stewart, Unconventional superconductivity, *Adv. Phys.* **66**, 75 (2017).
- [46] A. H. Castro Neto, G. Castilla, and B. A. Jones, Non-Fermi Liquid Behavior and Griffiths Phase in *f*-Electron Compounds, *Phys. Rev. Lett.* **81**, 3531 (1998).
- [47] B. Andraka and A. M. Tsvetlik, Observation of non-Fermi-liquid behavior in  $\text{U}_{0.2}\text{Y}_{0.8}\text{Pd}_3$ , *Phys. Rev. Lett.* **67**, 2886 (1991).
- [48] A. M. Tsvetlik and M. Reizer, Phenomenological theory of non-Fermi-liquid heavy-fermion alloys, *Phys. Rev. B* **48**, 9887 (1993).